



Calibration of cohesive parameters for a castable refractory using 4D tomographic data and realistic crack path from in-situ wedge splitting test

Rafael Vargas, Benjamin Smaniotto, Rodrigo Bresciani Canto, François Hild

► To cite this version:

Rafael Vargas, Benjamin Smaniotto, Rodrigo Bresciani Canto, François Hild. Calibration of cohesive parameters for a castable refractory using 4D tomographic data and realistic crack path from in-situ wedge splitting test. Journal of the European Ceramic Society, 2023, 43 (2), pp.676-691. 10.1016/j.jeurceramsoc.2022.09.040 . hal-03782687

HAL Id: hal-03782687

<https://hal.science/hal-03782687>

Submitted on 21 Sep 2022

HAL is a multi-disciplinary open access archive for the deposit and dissemination of scientific research documents, whether they are published or not. The documents may come from teaching and research institutions in France or abroad, or from public or private research centers.

L'archive ouverte pluridisciplinaire **HAL**, est destinée au dépôt et à la diffusion de documents scientifiques de niveau recherche, publiés ou non, émanant des établissements d'enseignement et de recherche français ou étrangers, des laboratoires publics ou privés.

Calibration of cohesive parameters for a castable refractory using 4D tomographic data and realistic crack path from in-situ wedge splitting test

R. Vargas^{a,c}, R.B. Canto^{a,b}, B. Smaniotto^c and F. Hild^c

^aFederal University of São Carlos, Graduate Program in Materials Science and Engineering (PPGCEM), 13565-905, São Carlos-SP, Brazil

^bFederal University of São Carlos (UFSCar), Department of Materials Engineering (DEMa), 13565-905, São Carlos-SP, Brazil, Brazil

^cUniversité Paris-Saclay, CentraleSupélec, ENS Paris-Saclay, CNRS, LMPS – Laboratoire de Mécanique Paris-Saclay, 91190 Gif-sur-Yvette, France

ARTICLE INFO

Keywords:

3D crack path

Parameter sensitivity

Cohesive Zone Model (CZM)

Digital Volume Correlation (DVC)

Finite Element Model Updating (FEMU)


Refractory castable

Wedge Splitting Test (WST)

ABSTRACT

Crack propagation in an alumina castable refractory with mullite-zirconia aggregates was investigated in-situ using a wedge splitting test setup performed inside a laboratory tomograph. Four-dimensional (*i.e.*, 3D space and time) data from digital volume correlation were used to investigate the influence of a realistic crack path on the simulation of the fracture process. A cohesive law was chosen, since toughening mechanisms were present, and calibrated via finite element model updating. When a straight crack path was assumed instead of the experimental crack path, a 10% higher fracture energy and a 35% higher cohesive strength were calibrated. Although the force alone could be used in the minimized cost function, the kinematic information gives valuable insight into the trustworthiness of the geometrical hypotheses assumed in the finite element model. Such framework can be applied to study nonlinear fracture processes for different materials with complex toughening mechanisms such as crack deflection or branching.

*Corresponding author

 r.vargas_m@ppgcem.ufscar.br (R. Vargas)

ORCID(s): 0000-0002-1711-9804 (R. Vargas); 0000-0002-9286-9912 (R.B. Canto); 0000-0001-5553-0066 (F. Hild)

1. Introduction

Several industries rely on processes involving high temperatures. For example, some containers are required to withstand thermomechanical stresses when in direct contact with molten glass or steel [1]. Castable refractories can be formed into such geometries and achieve the necessary properties [2] with properly engineered microstructures, which usually consist in coarse aggregates bounded by a finer matrix, both with special compositions and granulometry [3]. In these environments, it is common practice to deal with some levels of damage since it is impractical to avoid its initiation [4]. Therefore, studies concerning the formation and development of cracks together with their effect on mechanical properties are mandatory for material selection and design procedures.

Cohesive zone models (CZMs) were considered to describe the fracture of refractories. The cohesive law proposed by Hillerborg et al. [5, 6] was calibrated by Cotterell et al. [7] using Crack Mouth Opening Displacements (CMODs) to study thermal shocks. It was also used by Andreev and Harmuth [8] to simulate typical in-service thermomechanical loading cycles, and Jin et al. [9] to simulate a steel industry process. Gruber and Harmuth [10] also calibrated it using a disk test with laser illumination, achieving good agreements between simulated and experimental CMODs and acoustic emission results. Samadi et al. [11] proposed a similar damaged elasticity model to study the final stages of fracture in a wedge splitting test (WST) setup. Mathias and Tessier-Doyen [12] used the CZM proposed by Xu and Needleman [13] on the interface of a glass/alumina model material to study debonding. No details were given on the optimization procedure to calibrate the chosen parameters. Özdemir et al. [14] simulated interface debonding in thermal shock experiments with thermal gradients. A modified version of the previous CZM to better account for mode-mixed debonding [15] was calibrated via an inverse procedure considering the segmentation of the sample and the evaluation of the Young's modulus in different regions of the sample. Van Gils et al. [16] studied deviations from linear elastic fracture mechanics with cohesive laws in refractories, and Hein et al. [17] the influence of changing CZM parameters to simulate layered refractories under thermal shock. Both references utilized parameters with no experimental exploration.

Pan et al. [18] found the parameters of the (bilinear) CZM proposed by Alfano and Crisfield [19] using a nonlinear least-squares algorithm to minimize the difference between experimental and simulated loading curves. Doitrand et al. [20] carried out FE simulations for several combinations of CZM parameters and identified the best fit of force and crack length data. Vargas et al. [21] used CMOD data measured via DIC as boundary conditions to update finite element models with force data in the cost function (*i.e.*, FEMU-F) and later on coupled the notch opening displacement (NOD) in the cost function (*i.e.*, FEMU-F-NOD) for cases with restricted DIC field of view [22, 23]. Of the aforementioned references, only Refs. [22, 23, 20] used DIC to assess experimental boundary conditions.

A chevron notched graphite specimen loaded in-situ with a wedge in a lab tomograph [24] was analyzed via DVC. The crack front was determined by comparing experimental crack opening displacements (CODs) and simulations

with different prescribed positions before extracting stress intensity factors. The authors stated that the simulated CODs could be made closer to experimental CODs if cohesive elements were used. They subsequently proved their statement using a bilinear traction separation law [5] to analyze a new experiment with the same material and geometry performed in a synchrotron facility [25]. The simulated and measured CODs were compared to validate the selected model. Sensitivity analyses to the CZM parameters were discussed. The cohesive strength and fracture energy were extracted from independent experiments. Using cohesive elements along all grain boundaries was also performed to study the effect of grain orientation on intergranular local thermal stresses for polycrystalline alumina [26] by simulating its cooling from high temperatures. Diffraction contrast tomography was used to map the microstructure in the numerical simulations. DVC allowed the Poisson's ratio to be calibrated and the bending magnitude of the in-situ uniaxial compression test to be quantified.

Few studies can be found in the literature about the construction of cracked surfaces using 3D imaging techniques. Ferrié et al. [27] defined the crack path via manual segmentation along the reconstructed volumes (in the deformed configuration) to assess stress intensity factors (SIFs) along the 3D crack front of an Al-Li alloy. Rannou et al. [28] performed a multiscale mesh adaption on the DVC gray level residuals of a cast iron sample to compare SIFs evaluated via X-DVC and extended FE analyses driven by measured boundary conditions. In such approaches, the results are not only affected by measurement uncertainties but also by the chosen method to adapt the crack path [29]. The hypothesis of a straight crack path to obtain fracture parameters in a biaxial fatigue test in titanium alloys was analyzed in Ref. [30]. Such results were compared to the case using the real crack path obtained via microscopy and failure analysis with oscillations along the crack front and mode-mixities that were not present in the first case.

2. Experimental analyses

2.1. Studied castable and sample preparation

For the present study, the material was formulated and donated by IBAR (Indústria Brasileira de Artigos Refratários), located in Poá, Brazil, and consists of a low cement alumina castable refractory with fused mullite-zirconia aggregates. One SEM image of an unpolished sample is shown in Figure 1(a) to highlight the 3D aspect of the eutectic formation in mullite-zirconia aggregates. Such aggregates were shown to promote toughening mechanisms when cracks are deflected inside them for WSTs performed at 600°C [31], and to provide natural contrast to the matrix in tomographic acquisitions [31, 32], which is interesting for DVC purposes.

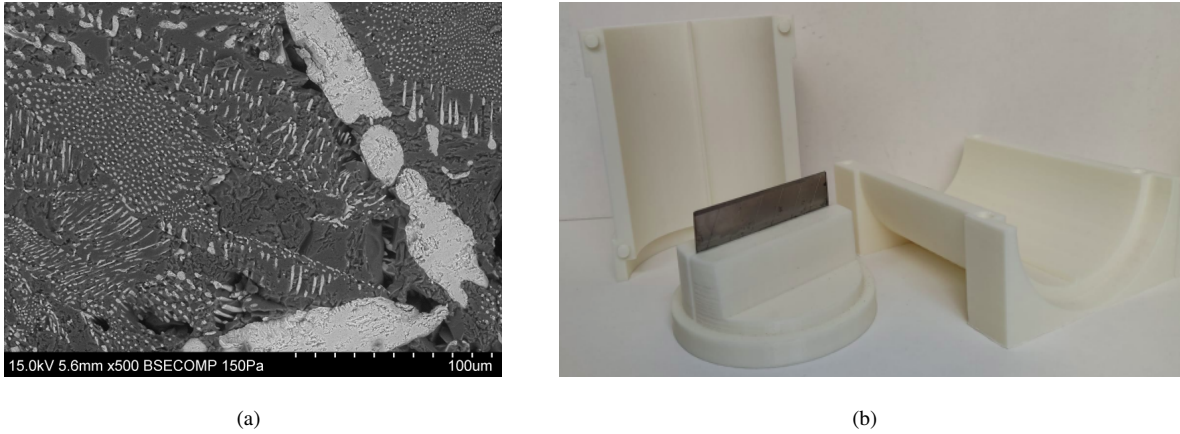


Figure 1: (a) Typical microstructure of the aggregates in the studied material. (b) Mold used to cast the WST sample.

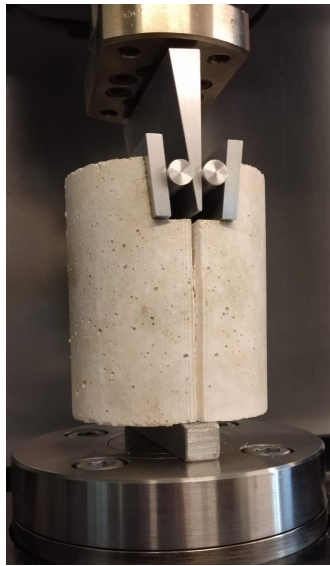
The mixture was homogenized after addition of 5.2% of water, and then poured in 3D printed molds [Figure 1(b)] on a vibratory table. Duct tape and wires were used to avoid leakage and deformation of the cylindrical molds during production of the samples. The fact that the sample geometry was close to a cylinder was due to the fact that X-ray tomography imaging was utilized. The thickness of traversed material by the X-ray beam was essentially independent of the angular position of the sample with respect to the detector. The pre-notch was made from a sawed snap off knife blade, and the lateral grooves from the mold geometry [Figure 1(b)]. The geometry of the loading region was kept the same as that of parallelepipedic samples [33] in order to use the same loading parts. The sample was then cured at room temperature and 80% relative humidity for 24 h before drying at 110°C for another 24 h. A pre-fire with a rate of 1°C/min up to 600°C was first performed followed by a dwell time of 5 h at 600°C. Then, the sample was heated first to 600°C at a rate of 3°C/min and second up to 1450°C at 1°C/min, and last held for more 5 h (at 1450°C). A region of the bottom surface of the sample was ground to decrease the roughness where it was in contact with the lower support during the experiment.

2.2. In-situ WST

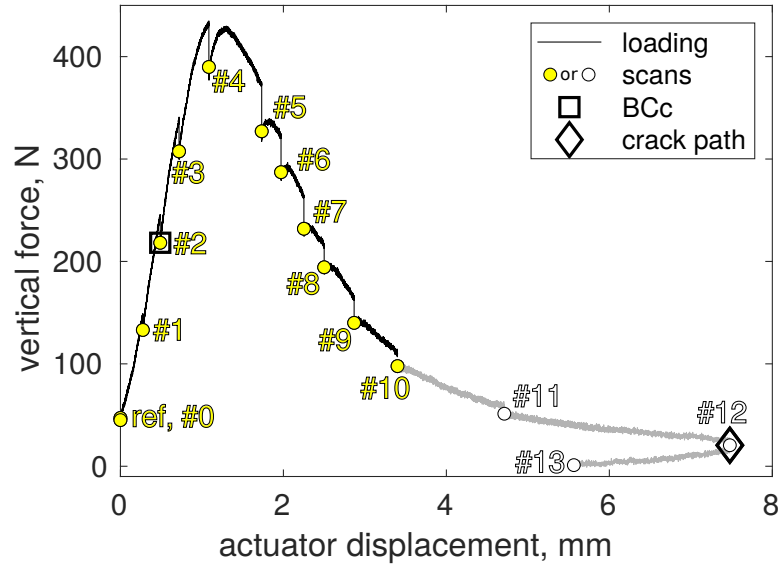
An *in-situ* monotonic wedge splitting [34] test on a cylindrical notched sample is analyzed hereafter. It was performed with the Deben TTC machine with a 20 kN load cell inside the NSI X50+ tomograph of LMPS. All the loading parts, namely, the wedge, two cylinders and two plates, were made of an aluminum alloy to allow for X-ray acquisitions in the loaded region (Figure 2(a)). For the wedge used herein with an angle $\theta = 5^\circ$ (between the wedge surfaces and the vertical axis), the applied (vertical) force (F_v) was amplified into two opposite (horizontal) splitting forces (F_h) by a factor of 5.715, according to $F_h = F_v / 2 \tan \theta$.

The loading curve is shown in Figure 2(b). Between scans, the loading was performed at constant stroke velocity of 1 $\mu\text{m/s}$. Once the targeted displacement was reached a dwell time of ≈ 5 min was selected prior to scanning. One

repeated scan was also performed in the reference state (with a pre-load of 50 N) to assess measurement uncertainties [35]. Results from the last three scans were not used as boundary conditions for the FE simulations since the chosen cohesive model was neither able to fully account for the final crack propagation stage nor unloading. However, the last scan before unloading (*i.e.*, scan #12, see Figure 2(b)) was considered to define the crack path as discussed in Section 4. Force drops are observed in Figure 2(b). Their largest part occurred during the dwell time prior to scanning. Such dwell time allowed most of the relaxation of the loading system to be accommodated. Smaller force fluctuations were observed during scanning. They are believed to be caused by minute displacements once rotating the turntable due to small misalignments in the setup (Figure 2(a)). [With the model calibrated herein, the (root mean squared) displacement variations for the maximum load drop (*i.e.*, ≈ 25 N in applied vertical force) were estimated to be equal to $3\text{ }\mu\text{m}$ or 2×10^{-2} vx, which was less than the DVC uncertainty level.]



(a)



(b)

Figure 2: (a) In-situ setup. (b) Loading curve for the monotonic *in-situ* WST. The disks depict when tomographic scans were performed; the yellow ones were used in the simulations. The square is the point considered for correcting the boundary conditions (Section 3.1) and the diamond the scan used for determining the crack path in the gray level residuals (Section 2.3.3). The gray points represent the part of the experiment that was not accounted for in the simulations. Scan numbers are indicated for easier referencing in the text.

2.3. DVC measurements

2.3.1. Principle

Finite element Digital Volume Correlation (DVC) was applied to extract displacement fields from tomographic volumes acquired during the experiment. Considering that the material points in the region of interest are present in

both the volume in the reference state f_0 and for that in the deformed configuration at time t_V , the gray level residual ρ reads

$$\rho(\mathbf{x}, t_V, \mathbf{u}) = f_0(\mathbf{x}) - f_{t_V}(\mathbf{x} + \mathbf{u}(\mathbf{x}, t_V)) \quad (1)$$

where the sought displacement field \mathbf{u} is discretized using 4-noded tetrahedra (*i.e.*, T4) elements (*i.e.*, $\mathbf{u}(\mathbf{x}, t_V) = \sum_i \Psi_i^{T4}(\mathbf{x}) u_i(t_V)$, where Ψ_i^{T4} refer to shape functions associated with T4-elements). The nodal displacements $u_i(t_V)$, which are gathered in the column vector $\{\mathbf{u}(t_V)\}$, are then determined by minimizing the L2 norm of the gray level residuals over the considered region of interest (ROI) with a Gauss-Newton scheme [36]

$$\{\mathbf{u}_{\text{DVC}}(t_V)\} = \arg \min_{\{\mathbf{u}\}} \sum_{\text{ROI}} \rho(\mathbf{x}, t_V, \{\mathbf{u}\})^2 \quad (2)$$

All the DVC analyses and post-processing were conducted in the Correli 3.0 framework [37]. The DVC parameters are gathered in Table 6 (Appendix A). By using FE-based DVC, the very same discretization can be used at the measurement and FE simulation stages to avoid interpolation errors and to fully exploit the experimentally measured forces.

2.3.2. Coarse mesh

From the geometry made after the nominal dimensions, a first coarse mesh was considered for DVC analyses. It was backtracked to best fit the actual sample shape as seen in the sections shown in Figure 3(a,b). It is worth noting that the microstructural scale of the SEM image shown in Figure 1(a) is not visible in the tomographic scans (Figures 3(a,b)) in which the mullite-zirconia aggregates appeared brighter than the matrix due to the higher atomic weight of zirconium, and the porosity darker. A voxelized mask associated with the nominal mesh was constructed with a gray level of 150 for the voxels inside the mesh and 30 gray levels otherwise. These values were the averages for the regions related to the sample or air (Figure 3(a)). One DVC analysis was then run by correlating this voxelized volume with the pre-loaded scan with an auxiliary hexahedron element that circumscribed the outer surface of the sample [38]. The displacement field at convergence was interpolated for the nodes of the nominal mesh, thereby allowing it to be backtracked for subsequent DVC analyses. All the meshes used herein, which were first drafted in the same coordinate system and created in GMSH [39], were then repositioned in the experimental reference configuration (*i.e.*, backtracked [38]) using the same displacements obtained from the preliminary registration with an auxiliary circumscribed mesh to ensure the same positioning for all of them.

The average element size (*i.e.*, cube root of mean element volume) of the coarse mesh was 27 vx, and a small mechanical regularization length $\ell_m = 10$ was used. The two surfaces where the splitting forces were applied (Figures 3(c) and 4) were described as Dirichlet boundaries for which the high frequency fluctuations of the tractions were filtered out [40]. The splitting displacement (*i.e.*, in the x -direction) is shown for the scan with the largest actuator

displacement in Figure 3(c) after the rigid body motions were removed. A displacement amplitude of about ± 6 vx (or ≈ 0.8 mm) occurred in the region where the splitting forces were applied. The reference and deformed volume for this analysis together with its voxelwise residual volume are shown in the supplementary data. When using this coarse mesh, the standard displacement uncertainty was $\sigma_u = 1$ cvx (*i.e.*, ≈ 1.3 μ m), which was assessed as the standard deviation of the nodal displacements measured with the repeated scan acquired in the pre-loaded configuration (*i.e.*, scans ref and #0, see Figure 2(b)). Thanks to the small uncertainty levels, the displacements measured with this mesh were chosen to be used as boundary conditions in FE simulations.

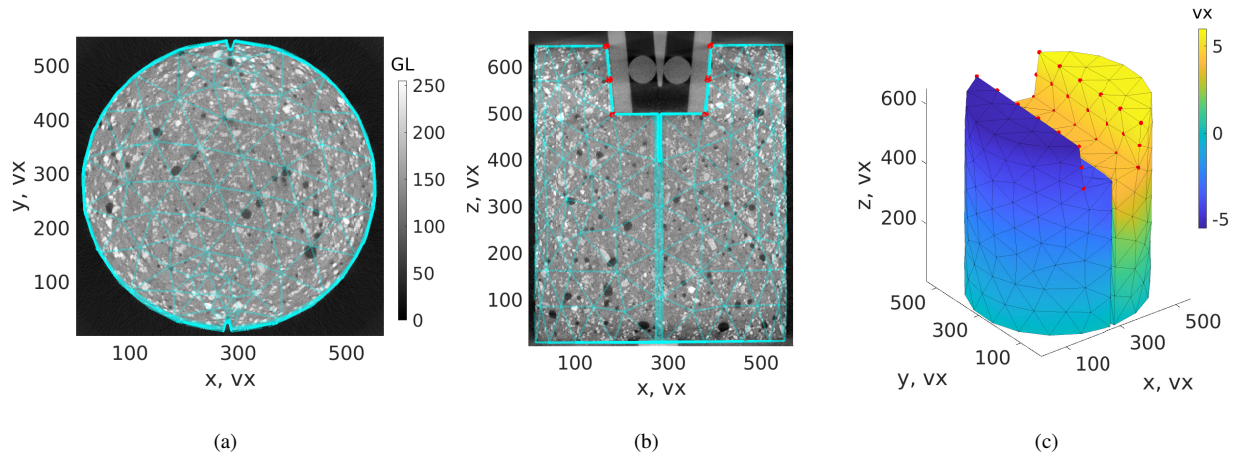


Figure 3: Coarse mesh shown in the x – y (a) and x – z (b) planes for the reference configuration. (c) Measured displacement field (expressed in vx) in the x -direction for the most loaded state. The red circles depict the nodes considered for Dirichlet nodes in the mechanical regularization scheme

2.3.3. Fine meshes

In order to use cohesive zone models, suited meshes are needed. A first fine mesh was obtained by implementing a straight vertical plane between the lateral grooves of the sample (Figure 4(a)). The average element size was reduced to 18 vx, with an average length of 10 vx for the triangles composing the cohesive elements, chosen after checking that further refinement did not improve the results. A second mesh was constructed (Figure 4(b)) by adapting the cohesive elements to the cracked surface detected in the gray level residuals of the DVC analysis using the coarse mesh for the scan with the most opened crack (*i.e.*, scan #12, see Figure 2). A similar approach was used in Ref. [28] to define the level set associated with crack surface thanks to the gray level residuals.

To illustrate the procedure to obtain meshes adapted to the crack path, the absolute gray level residual for scan #12 is shown in Figure 4(c) for the same x – z section as that of Figure 3(b). For each z -coordinate of a given x – z section below the initial notch, the x -position of the maximum residual was determined to adapt the mesh. An identical procedure was followed for all the other x – z sections. These positions were slightly corrected by setting all values outside the

physical visualization of the crack (*i.e.*, for x -coordinates less than 250 or greater than 350 vx, see Figure 4(c)) to the straight crack coordinates. Such corrections took place mostly for $z < 100$ vx where the crack opening displacement was very small. The open crack for the chosen scan makes it easier to define the cracked surface, although its front is not very clear as seen in low gray level residuals in the lower region of the adapted plane, which is represented in the $y - z$ -projected section in Figure 4(d). The x -coordinates of the crack plane were first adjusted by fitting the cohesive (surface) mesh to the identified crack surface without changing y and z coordinates. Then, the nodal x -coordinates were adapted in the 3D mesh (Figure 4(b)) by elastically deforming it, applying zero displacement on the external surfaces and the required displacement to the nodes of the cohesive surface. It is worth noting that in DVC analyses the split nodes remained uncoupled.

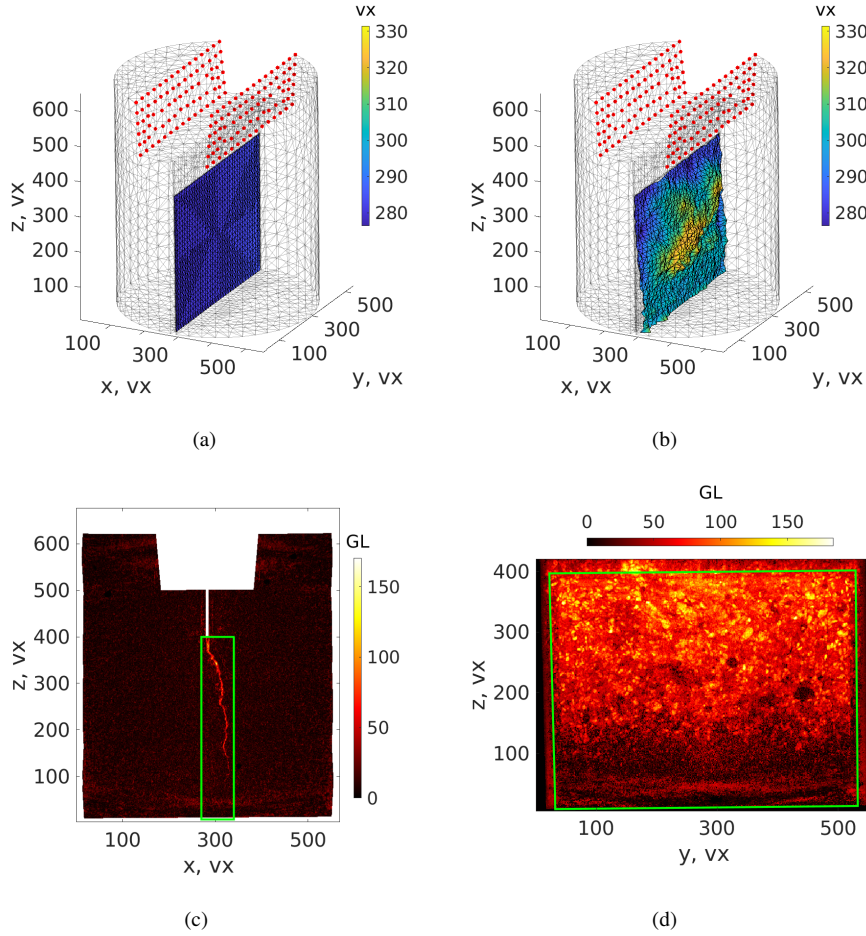


Figure 4: Elements at the surface of the finer meshes used in FE simulations with cohesive elements on a perfect plane (a), or adapted to the crack surface (b) from the analysis of $x - z$ sections of the DVC residuals (c), in which their positions for the final crack path are shown in sub-figure (d). The color bar in sub-figures (a,b) encodes the node position in the x -direction and the absolute gray level of the voxel-wise DVC residual in sub-figures (c,d). The red circles depict Dirichlet nodes in the mechanical regularization scheme and as boundary conditions in FE simulations. The green box highlights the area where the gray level residuals were calculated to probe the trustworthiness of the two considered crack paths

3. Mechanical simulations

3.1. Boundary conditions

The measured displacements were prescribed as Dirichlet boundary conditions on the nodes of both surfaces where the splitting force was applied (Figures 3(c) and 4(a,b)). In order to mitigate the influence of measurement uncertainties, the displacements measured with the coarser mesh were interpolated on the nodes of the finer meshes. With the chosen scans, the last step in the FE simulations corresponds to an applied force of the order of 20% of the ultimate load (*i.e.*, scan #10, see Figure 2(b)).

Moreover, the reference scan was not acquired in the fully unloaded state. Thus, the displacement field from the unloaded to the pre-loaded states was unknown. The BCc (*i.e.*, Boundary Condition correction) parameter was added in the identification scheme to account for this fact [21]. This parameter was defined as one scalar that multiplies the boundary conditions from the scan at 50% of the ultimate load prior to reaching the ultimate load (*i.e.*, scan #2, see Figure 2(a)). If such parameter is equal to one, it means that no correction was necessary, while above unity represents an opening and below one a closure correction field. For example, if the calibrated parameter is equal to 1.2, it indicates that 20% of the boundary condition measured for the time step defined in the parameter (*i.e.*, scan #2) was used to approximate the unknown initial boundary condition.

3.2. Constitutive models

Both meshes shown in Figure 4 were considered in the sequel. Each P6 cohesive element was combined by considering one triangular element from each side of the crack mouth. An Abaqus user element was selected for the so-called PPR model [41, 42]. The initial stiffness parameter α was equal to 0.005 for numerical stability, and the shape parameter $\lambda = 7$ due to its suitability to the present material [31]. The parameters of the traction-separation law are the cohesive strength σ_f , and the fracture energy J_c , since they were considered identical for every mode. For the remainder of the sample, C3D4 elements were used with a linear elastic behavior.

3.3. Identification procedure

The chosen identification procedure is the so-called Finite Element Model Updating (FEMU) procedure [43, 44, 45], which consists in first defining an FE model and then iteratively updating its parameters in order to best fit the computed variables to experimental data. This section discusses the required points for such technique, apart from the geometry, boundary conditions, and constitutive models that were previously introduced.

3.3.1. Finite element model updating

The calibration proceeds by minimizing the sum of normalized squared differences χ^2 , which may comprise different cost functions using different experimental quantities. In the present case, weighted cost functions were considered in which the standard uncertainty γ associated with any data set was considered [46]. Within such setting, $\chi \rightarrow 1$ when the only random source of error is related to measurement uncertainties. Any departure from 1 signals a model error.

Hereafter, four experimental data sets were considered, namely, the horizontal splitting force F (*i.e.*, 5.715 times the applied vertical force)

$$\chi_F^2(\{\mathbf{p}\}) = \frac{1}{N_{t_F}} \sum_{t_F} \left(\frac{F_m(t_F) - F_{FE}(t_F, \{\mathbf{p}\})}{\gamma_F} \right)^2, \quad (3)$$

the nodal displacement vectors $\{\mathbf{u}(t_u)\}$

$$\chi_u^2(\{\mathbf{p}\}) = \frac{1}{3N_{t_u}N_n} \sum_{t_u} \sum_n \left(\frac{u_m(t_u, n) - u_{FE}(t_u, \{\mathbf{p}\}, n)}{\gamma_u} \right)^2, \quad (4)$$

the nodal crack opening displacement along the x -direction

$$\chi_{COD}^2(\{\mathbf{p}\}) = \frac{1}{N_{t_u}N_{nc}} \sum_{t_u} \sum_{nc} \left(\frac{COD_m(t_u, n_c) - COD_{FE}(t_u, \{\mathbf{p}\}, n_c)}{\gamma_{COD}} \right)^2 \quad (5)$$

and the gray level residuals

$$\chi_\rho^2(\{\mathbf{p}\}) = \frac{1}{N_{t_V}N_{ux}} \sum_{t_V} \sum_{\mathbf{x}} \left(\frac{f_0(\mathbf{x}) - f_{t_V}(\mathbf{x} + \mathbf{u}_{FE}(t_V, \{\mathbf{p}\}, \mathbf{x}))}{\gamma_\rho} \right)^2 \quad (6)$$

All the previous expressions depend on the sought parameters that gathered in the column vector $\{\mathbf{p}\}$, and listed in Section 3.3.4. Since in this type of experiment it is usual practice to have different acquisition frequencies for these quantities, different time steps t were considered, as explained in the next section. Once normalized, they are assembled in a single cost function

$$\chi_{tot}^2 = \omega_F \chi_F^2 + \omega_u \chi_u^2 + \omega_{COD} \chi_{COD}^2 + \omega_\rho \chi_\rho^2 \quad (7)$$

in which the various weights ω were selected following the sensitivity analysis presented in the sequel. For instance, if $\omega_F = 1$ and the other three weights cancel out, then it corresponds to FEMU-F. The case ω_F and ω_u both different from zero is related to FEMU-UF. Equivalently, ω_F and ω_{COD} also refers to FEMU-UF in which the kinematic cost function only focuses on the displacement jumps, which are one key quantity for cohesive zone models. Last, integrated DVC requires ω_F and ω_ρ to be the only non vanishing weights.

3.3.2. Temporal discretization

In the present FEMU approach, a total of twelve tomographic scans was used (*i.e.*, from scans #0 to #10, thus $N_{t_V} = 11$). The first two were acquired in the pre-loaded state, which was considered as the reference configuration. To enrich the temporal description of the FE kinematics, more time steps than those of the DVC calculations were used for the boundary conditions. Between two consecutive tomographic scans, four more points were linearly interpolated (*i.e.*, $N_{t_u} = 51$). Therefore, for the applied boundary conditions, 11 time steps were measured via DVC while the other 40 were interpolated to force at which time increment FE data would be gathered. Moreover, all acquired force data during loading of the sample between tomographic scans were accounted for in the minimization procedure. The forces calculated in the 51 simulation steps were linearly interpolated to get the same number (*i.e.*, $N_{t_F} = 11,368$) of data points.

3.3.3. Measurement uncertainties

The measurement uncertainties used to normalize the cost functions are reported in Table 1. The standard force uncertainty γ_F was calculated from the standard deviation of acquisitions before the experiment (and then multiplied

by 5.715 to assess the splitting force uncertainty). The standard displacement uncertainties γ_u and γ_{COD} were assessed from the standard deviation of the DVC measurements between the two scans in the reference configuration. Similarly, γ_ρ corresponds to the standard deviation of the gray level residuals after correlating both scans in the reference configuration.

Table 1

Standard measurement uncertainties for the four data sets

Quantity	Standard uncertainty γ
F [N]	8
u [cvx/ μm]	3 / 4.0
COD [cvx/ μm]	7 / 9.4
ρ [gray level]	9.7

3.3.4. Initialization

The Young's modulus E , together with the cohesive parameters σ_f , J_c , and the BCc parameter were calibrated via FEMU. They were initialized according to values previously obtained for such material, which are gathered in Table 2, in which E was taken from Ref. [23], σ_f and J_c from Ref. [31], and BCc was initialized as if no boundary condition correction were needed (*i.e.*, BCc = 1).

Table 2

Initial parameters for the FEMU-F analyses

Parameter	Description	Initial value
E [GPa]	Young's modulus	46
BCc	Boundary condition correction	1
σ_f [MPa]	Cohesive strength	4.3
J_c [J/m ²]	Fracture energy	270

3.3.5. Sensitivity analysis

The sensitivity S_F of the calculated force and COD (S_{COD}) on each parameter was assessed in order to choose the weighting for the cost function to be minimized (see Equation (7)). Only the case with the fine mesh adapted to the DVC residuals is discussed. The (rectangular) sensitivity matrices were computed via finite differences using a 1% perturbation to each initial estimate of the parameters $\{\mathbf{p}_0\}$ (see Table 2)

$$\left[\hat{\mathbf{S}}_F\right] = \frac{1}{\gamma_F} \left[\delta F_{\text{FE}}(t, \{\mathbf{p}_0\})\right] \quad \text{and} \quad \left[\hat{\mathbf{S}}_{\text{COD}}\right] = \frac{1}{\gamma_{\text{COD}}} \left[\delta \text{COD}_{\text{FE}}(t, \{\mathbf{p}_0\})\right] \quad (8)$$

where each matrix was constructed from the concatenation of column vectors gathering all variations (using the δ symbol) for a given parameter. Consequently, the size of the load sensitivity matrix $[\hat{\mathbf{S}}_F]$ is $N_{t_F} \times 4$, and that of $[\hat{\mathbf{S}}_{\text{COD}}]$ is $(N_{t_u} N_{n_c}) \times 4$. When normalized by the standard measurement uncertainty, the dimensionless sensitivity matrices correspond to Signal to Noise Ratios (SNR) representing how many times the fluctuations (induced by a 1% increment in the parameters) vary with respect to the measurement uncertainty for each time step. To illustrate such analysis, the force sensitivities $\hat{\mathbf{S}}$ are shown in Figure 5.

With the selected normalization, it is straight forward to check if fine tuning any sought parameter would be conceivable. In the present case, all of them reached sensitivities at least three times the uncertainty level at some time steps (*i.e.*, an absolute SNR of 3). Moreover, it is observed that their temporal changes were weakly correlated, which is an additional benefit for the minimization scheme.

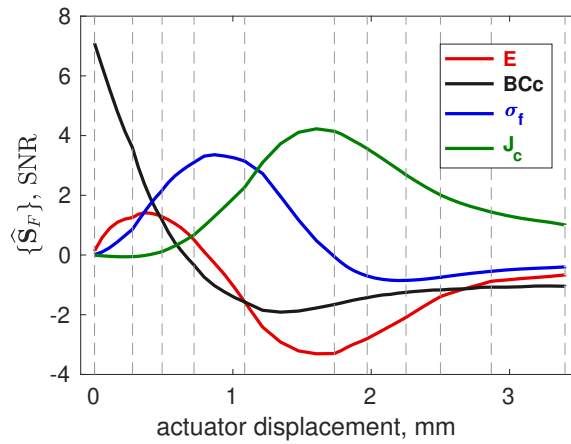


Figure 5: Force sensitivities for the initial set of parameters after a 1% perturbation normalized by the force uncertainty. The vertical dashed lines depict the tomographic scans

The COD sensitivity fields $\hat{\mathbf{S}}_{\text{COD}}$ are displayed in Figure 6 with levels at least two orders of magnitude lower than $\hat{\mathbf{S}}_F$ (Figure 5). In the present case, only the component along the x -direction is reported; the other components were about 5 times lower. Positive values mean that an increase of the parameter increased more the opening, while a negative sensitivity was related to less opening. One interpretation of such fields is that, in order to reduce the COD residual one time the standard uncertainty, it would be necessary to have changes of at least 50% in the sought parameters. Moreover, considering the force and COD sensitivities, if they were coupled in the cost function, such calibration would be guided mostly by force measurements with equivalent weightings.

The COD sensitivity for the Young's modulus (first row in Figure 6) indicates that an increase on this parameter led to further opening in the crack, since a higher elastic energy could make crack initiation and propagation easier. Low sensitivities occurred for the first time steps, while this parameter had the strongest influence for scan #5 (*i.e.*, right after the ultimate load). The opening trend was qualitatively similar for the BCc parameter (second row in Figure 6)

due to the fact that when it increased, the prescribed load increased, thereby opening the crack. For BCc parameter, the crack opening fields stabilized after scan #4, with similar sensitivity afterward. From these two sensitivity fields it was possible to infer that the opening was not entirely symmetric at the beginning of the test, with higher openings at the side with smaller y -coordinate. When the cohesive strength (third row in Figure 6) increased, the crack was closed at the beginning, since crack initiation was delayed. Conversely, an opening trend is observed at later time steps since propagation would then be at an advanced stage, once smaller openings were required for higher damage levels (*i.e.*, the maximum separation required for full failure of the elements is decreased). The SNR range associated with this parameter was the lowest, which indicates that it had the least sensitivity. Last, for the fracture energy (fourth row in Figure 6), the sensitivity was very low at the beginning (*i.e.*, prior to scan #4), but tended to close the crack since when J_c was increased, more energy was needed to open the crack. It is worth noting that such sensitivities are shown for the initial parameter set (see Table 2) and may change during the iterative scheme due to parameter interdependence.

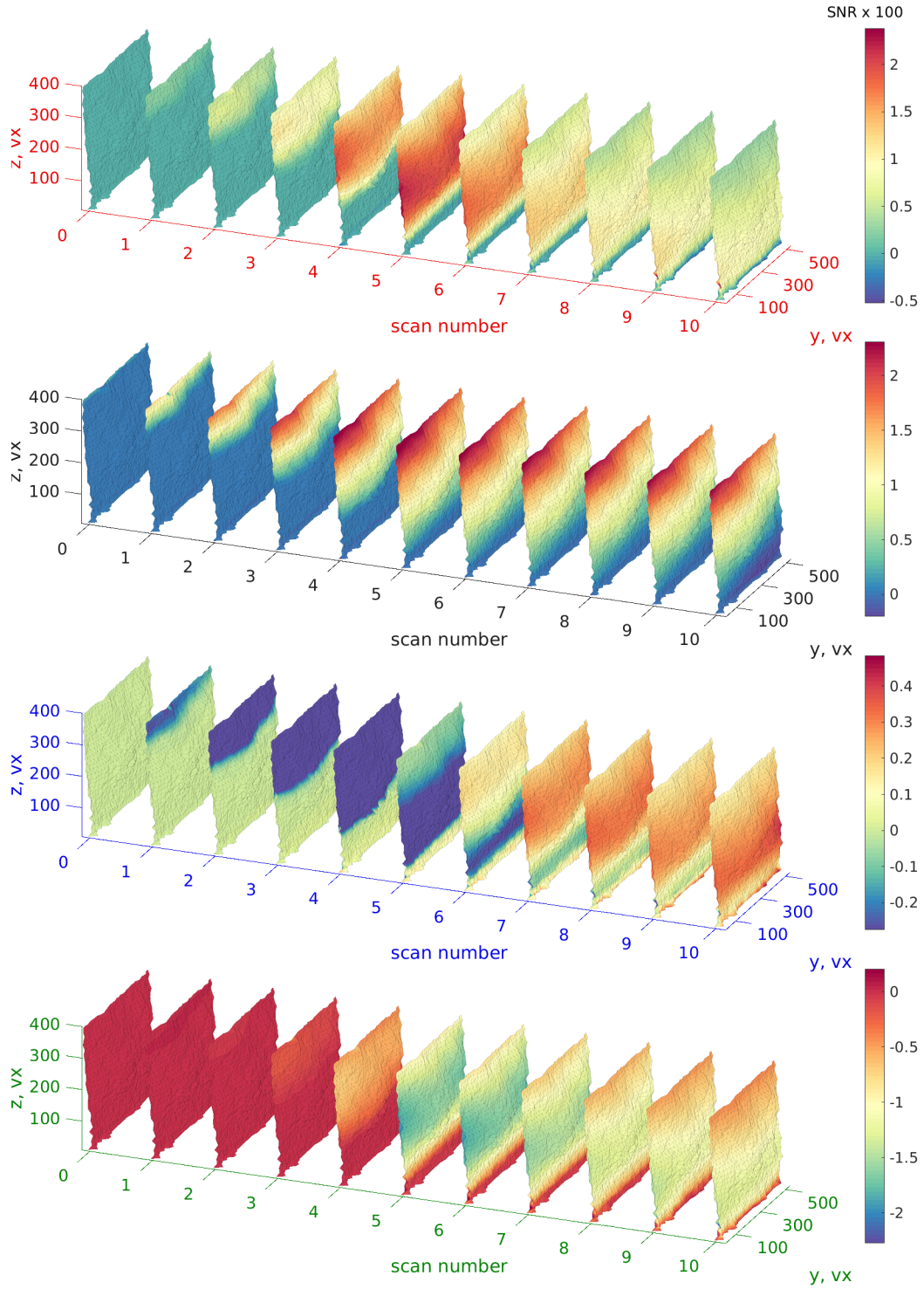


Figure 6: Sensitivity fields \hat{S}_{COD} for the displacement jump in the x-direction for a 1% variation of the parameters E (top row), BCc (second row), σ_f (third row), and J_c (bottom row)

The sensitivities can be further understood by analyzing the respective Hessian matrices

$$[\hat{\mathbf{H}}_F] = \frac{1}{N_{t_F}} [\hat{\mathbf{S}}_F]^\top [\hat{\mathbf{S}}_F] \quad \text{and} \quad [\hat{\mathbf{H}}_{\text{COD}}] = \frac{1}{N_{t_u} N_{nc}} [\hat{\mathbf{S}}_{\text{COD}}]^\top [\hat{\mathbf{S}}_{\text{COD}}] \quad (9)$$

whose absolute values are shown in decimal logarithm in Figure 7 together with their respective eigen decomposition. First, the condition number of the force Hessian matrix (Figure 7(a)) is three orders of magnitude smaller than that of the COD (Figure 7(d)), *i.e.*, 1.3×10^2 in comparison to 4.9×10^5 , which will lead to a more stable identification with the former. Moreover, the way the sensitivities were calculated (Equation (8)), the Hessian matrices are interpreted as average changes in squared SNRs. Therefore, apart from the coupling between of the cohesive strength σ_f to the parameters E or BCc , all the other Hessian values indicate an average sensitivity above unity. The weakest eigen parameter indicates that its sensitivity is not strong enough to completely decouple E from J_c (see their negative correlation in Figure 5), and that the sensitivity to E is smaller.

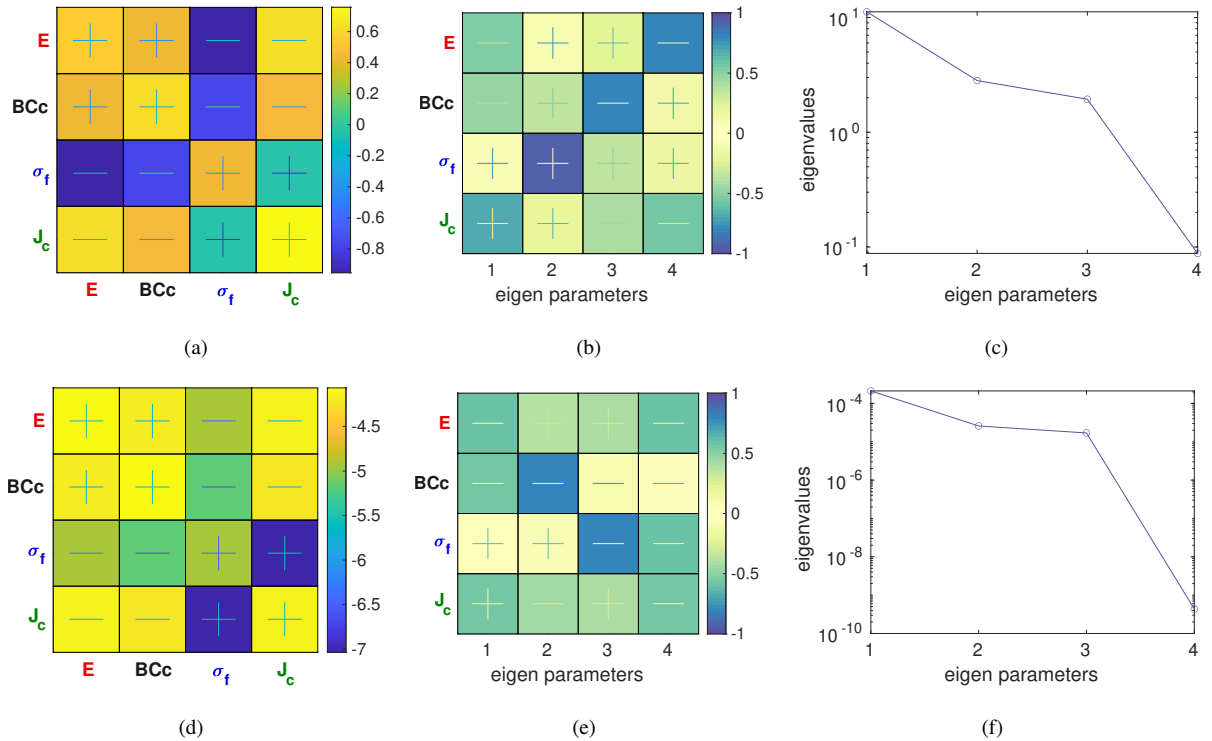


Figure 7: Normalized Hessians in decimal logarithm (a,d) together with their eigen decomposition. The eigen parameters are shown in subfigure (b,e) and eigenvalues in (c,f). Results related to force measurements are shown in the first row and to COD data in the second row.

For the COD Hessian matrix (Figure 7(d)), not only the condition number is higher but also the overall levels are considerably smaller, by more than three orders of magnitude, showing that in average the sensitivity is below the uncertainty levels. The weakest eigen parameter (Figure 7(e,f)) corresponds to a coupling involving all the sought

Calibration of cohesive parameters for a refractory using 4D data and realistic crack path from in-situ WST parameters and with an eigenvalue of five orders of magnitude lower than its force peers, which indicates that these four parameters cannot be identified if only COD data were available. The same conclusion applied for full displacement fields (Appendix B) and gray level residuals.

Consequently the minimization procedure was simplified (*i.e.*, $\omega_F = 1$, and $\omega_u = \omega_{\text{COD}} = \omega_\rho = 0$) by iteratively updating the current estimate of the parameters by solving linear systems

$$[\mathbf{H}_F] \cdot \{\delta \mathbf{p}\} = \{\mathbf{h}_F\} \quad (10)$$

where the right hand member $\{\mathbf{h}\}$ reads

$$\{\mathbf{h}_F\} = [\mathbf{S}_F]^\top \{F_m(t_F) - F_{\text{FE}}(t_F, \{\mathbf{p}_n\})\} \quad (11)$$

and the sensitivity and Hessian matrices are no longer normalized as before (Equations (8)) and (14))

$$[\mathbf{H}_F] = [\mathbf{S}_F]^\top [\mathbf{S}_F] \quad \text{with} \quad [\mathbf{S}_F] = \left[\frac{\partial F_{\text{FE}}}{\partial \{\mathbf{p}\}}(t, \{\mathbf{p}_0\}) \right] \quad (12)$$

The iterative procedure stopped when the root mean square of the relative corrections $\{\delta \mathbf{p}\}$ was less than 0.01. The maximum increment allowed per iteration was 0.2 for each parameter.

Although the kinematic cost functions, or that related to the gray level residuals, were not used in the calibration procedure, they were assessed for each iteration and are discussed hereafter.

4. Results and discussion

4.1. FEMU-F calibration

First, the case with the straight crack (Figure 4(a)) is discussed. The calibration procedure converged in seven iterations even the initial guess was far from the final set of parameters. The horizontal force for each FEMU-F iteration is shown in Figure 8(a). The fact that for each iteration the calculated force became closer and closer to the experimental reference is proven by the significant reduction of the cost function χ_F (Figure 8(b)), namely, from 150 to seven times the standard force uncertainty. The change of parameters normalized by their converged level is displayed in Figure 8. The Young's modulus was the farthest from the final solution, whereas the other parameters had no more than 30% offsets.

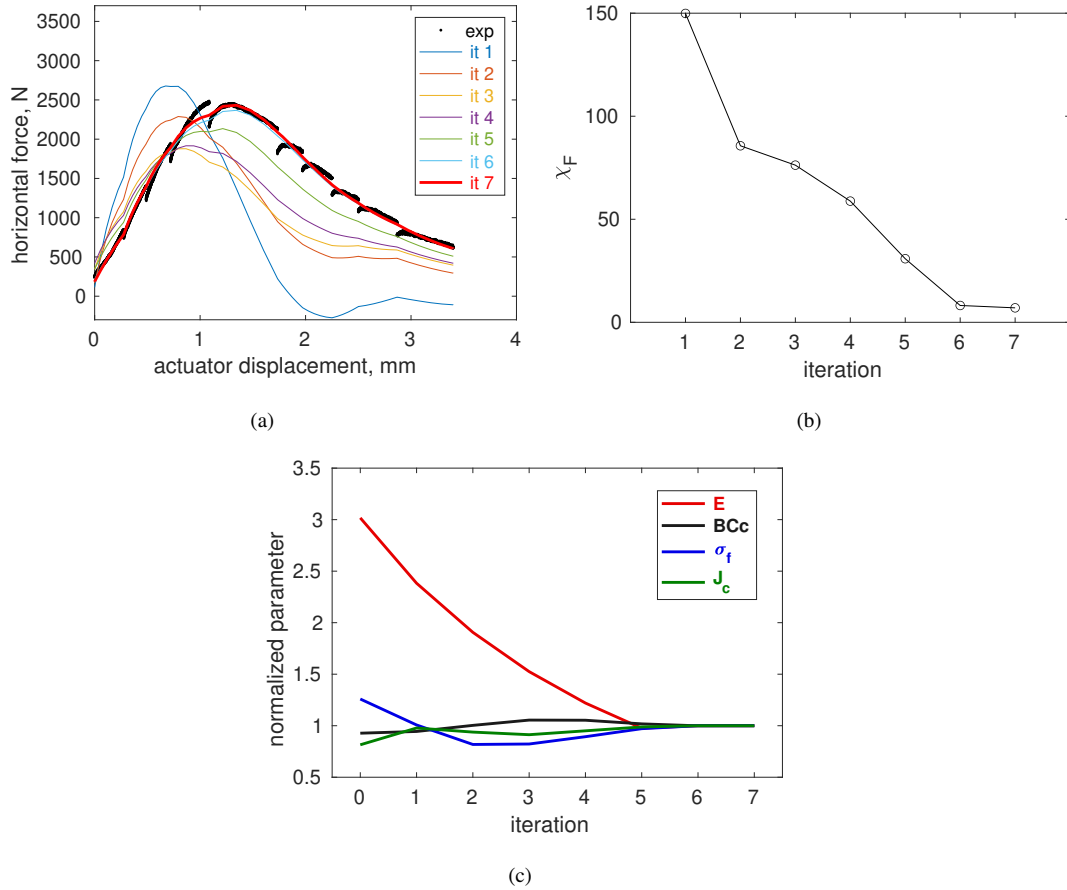


Figure 8: Results for parameter calibration on the case with straight crack path (Figure 4(a)). Loading curves (a), global force residual χ_F (b), and calibrated parameters (c) for each iteration

The same calibration procedure was applied with the cohesive elements adapted to the crack path (Figure 4(c)). The loading curves for each iteration are shown in Figure 9. Although the calibration also converged in seven iterations, the first one, with the same initialization as in the previous case, reached an ultimate splitting force about 1000 N higher than in the previous case. This observation reinforces the critical role of the crack path description for such identifications, since it was the only difference between these two cases. The global force residual χ_F was drastically reduced (Figure 9(b)), yet with very similar initial and final levels when compared to the first case. For the normalized parameters displayed in Figure 9(c), the biggest difference is seen in terms of the cohesive strength σ_f , which was lowered compared to the first case. This point indicates that this parameter was the most sensitive to the crack path, which is related to crack initiation.

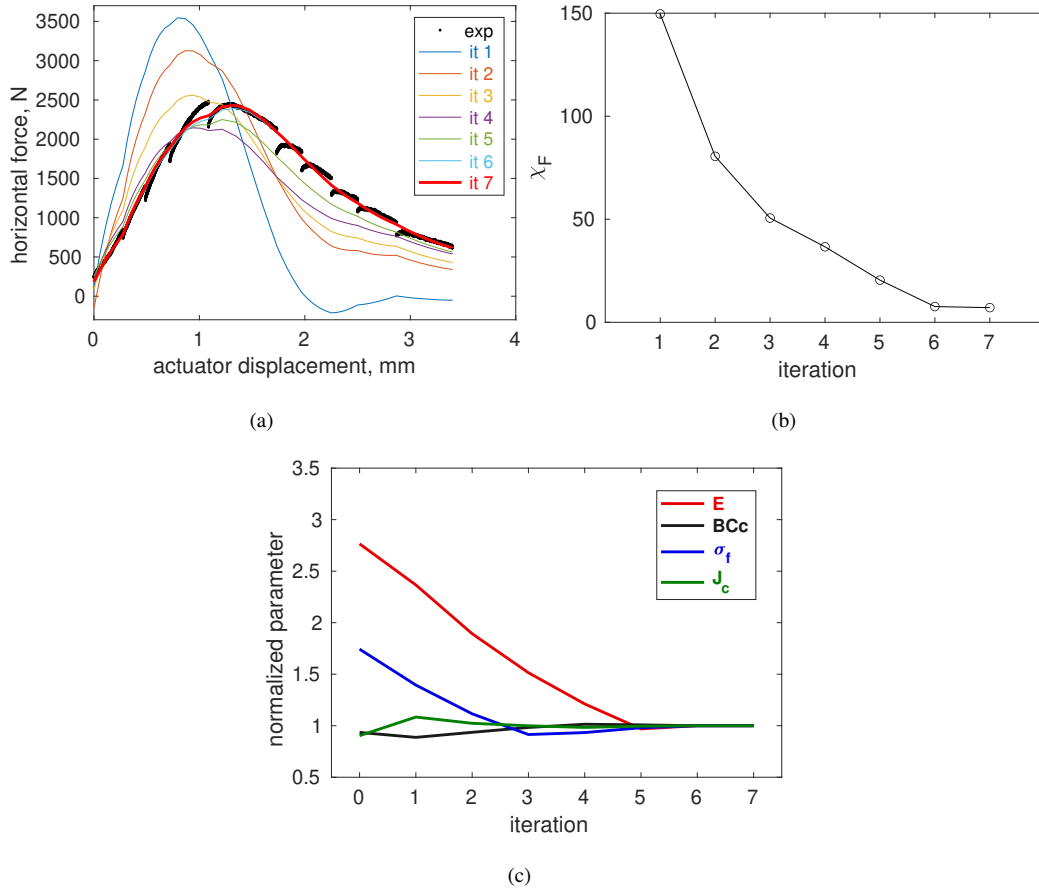


Figure 9: Results for parameter calibration on the case with adapted crack path (Figure 4(b)). Loading curves (a), global force residual χ_F (b), and calibrated parameters (c) for each iteration

The calibrated parameters are gathered in Table 3. The Young's moduli were less than 10% different between both cases, but about one third of the initial guess. Although more samples would be necessary to confirm this point, the sample processing may induce such reduction as more porosity was observed in the cylindrical samples in comparison to prismatic geometries made of the same material [33]. To improve this point, the mold sealing may be changed to lower the possibility of air coming in during consolidation on a vibrating table. The parameter BCc was very close as expected since the same DVC results from the coarse mesh were used as boundary conditions (Figure 4(a,c)).

Table 3

Calibrated parameters for the two crack paths

Parameter	Straight crack	Adapted crack
E [GPa]	16	17
BCc	1.08	1.07
σ_f [MPa]	3.4	2.5
J_c [J/m ²]	325	295
χ_F	7.0	7.1

The cohesive strength was almost 40% higher for a straight crack path, which led to the highest difference between all considered parameters. Interestingly, Ref. [31] discussed the fact that a value between 50% and 60% of the so-called nominal tensile strength was a good initialization for σ_f using the same material but with a different geometry. For the present experiment, it corresponds to 4.6 MPa, of which 55% of it leads to 2.5 MPa (*i.e.*, the same value calibrated for the adapted mesh). The fracture energy was also 10% higher for a straight crack path. The PPR traction-separation law is plotted in Figure 10 using the initialization and converged cohesive parameters to highlight the influence of geometry of the crack surface on their calibration.

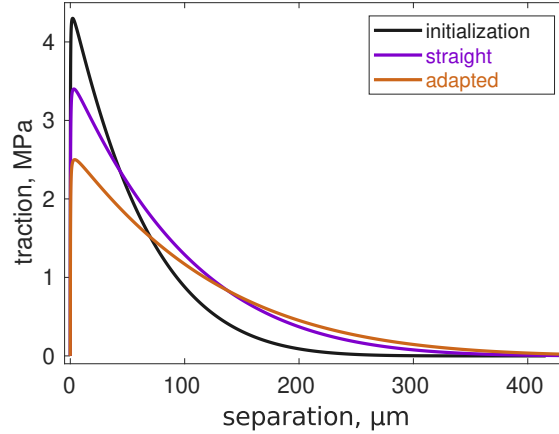


Figure 10: PPR traction-separation law using the initial parameters σ_f and J_c (Table 2) or the converged ones (Table 3) for both studied meshes

One final point is that both meshes resulted in very similar descriptions of the loading curve (*i.e.*, with a χ_F difference of 0.1 well below the uncertainty level). At this point, it would not be reasonable to discard any of the results. The kinematic cost functions that were not used in the calibration procedure will provide further insight into the faithfulness of the calibrations at more local levels.

4.2. Kinematic residuals

Although not directly used in the calibration procedure, the cost functions associated with displacement fields were investigated to further check the faithfulness of the FE simulations. First, the gray level residuals are presented in Figure 11(a). The higher residuals around scan #5 are related to the tomograph dark field correction that could only be acquired at the beginning and at the end of the experiment. This evaluation was possible for FE analyses since the experimentally measured boundary conditions were considered. When the FE kinematics was employed to correct the tomographic volumes in the deformed configurations, the global residual was higher than those obtained via DVC. However, it is worth noting that they remained very close, especially considering all the kinematic constraints enforced in the finite element simulations. The mesh adapted to the crack surface yielded lower levels than that with a straight crack path on both cases (DVC analyses and FE simulations), due to its better description of the fracture process. Moreover, when DVC analyses are compared, the residual from the coarse mesh was almost the same as the others at the beginning of the test but started to deviate from scan #3 onward. This phenomenon is due to crack propagation since no discontinuity was accounted for in the coarse mesh, while more degrees of freedom were used to improve the description of the kinematics in the vicinity of the crack for the finer discretizations.

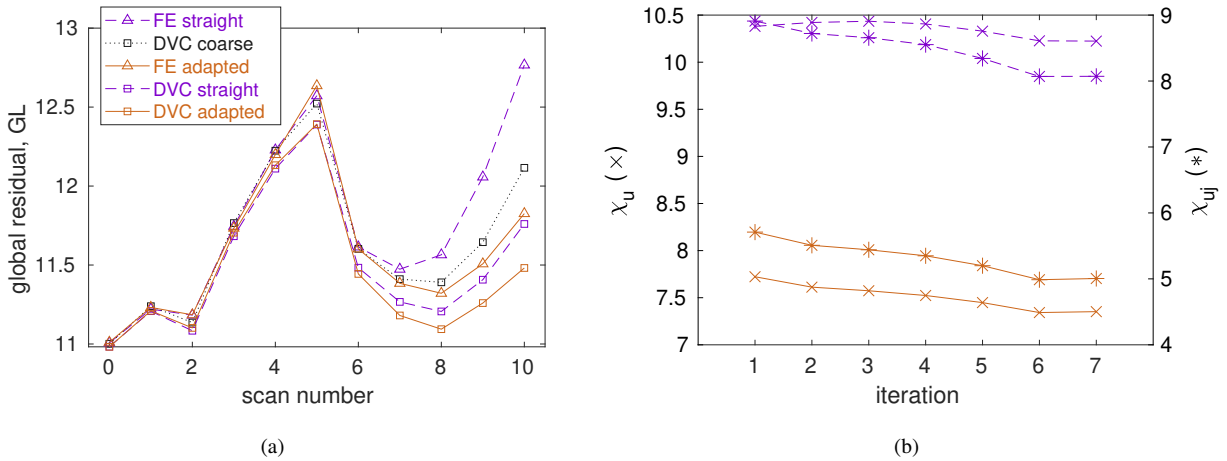


Figure 11: (a) Gray level residuals for DVC analyzes using different meshes (squares) or FE simulations driven by measured boundary conditions (triangles). (b) Cost functions using full displacement fields (χ_u , depicted with crosses) or only the crack opening displacement in the x -direction (χ_{uj} , depicted with stars). The black dotted line depicts the analysis using the coarse mesh (Figure 3), while dashed and solid lines represent the usage of meshes with a straight crack path or adapted to the real crack path, respectively (see Figure 4).

The cost functions associated directly with displacements are shown in Figure 11(b). Although they were not minimized, they were *also* lowered during the calibration procedure, further validating the way the mesh was positioned and boundary conditions were defined. They were already closer to one (*i.e.*, with levels less than eleven times the

Calibration of cohesive parameters for a refractory using 4D data and realistic crack path from in-situ WST standard uncertainties) for the initial guess in comparison to the force residuals (*i.e.*, about 150 times). With this metric, the mesh adapted to the crack geometry better performed than that with a straight path by three units using full displacement fields or only the crack opening displacement. This point proves that the adapted crack path provided a better description of the experiment at the macroscopic level (with force data), mesoscopic scale (with displacement data) and at the microscopic level (with gray level residuals), and therefore the corresponding parameters are more representative for the analyzed sample.

The displacement jump residuals at convergence of FEMU-F are shown in Figure 12. Such residuals (Figure 12) gives direct access to the displacement jumps the selected CZM cannot explain. Up to scan #4, the levels were really low and then slightly increased, reaching up to 10 or more in certain points. The high frequency oscillations are related to material heterogeneities. In order to decrease such residuals in the final steps, different CZMs are required in which the crack would need to be opened more near the notch root, and closed around the middle height. However, such changes may degrade the force residuals. For instance, when a single FEMU iteration was run with the converged parameters as initial guess but only considering the COD data in the cost function [*i.e.*, $\omega_{\text{COD}} = 1$ and $\omega_F = \omega_u = \omega_\rho = 0$ in Equation (7)], χ_{COD} was reduced by 0.01 while χ_F increased from 7 to 52 (with similar trends on following iterations). Such oscillations may be reduced using a Tikhonov regularization [47]. From the low residuals obtained herein, it is believed that the current simulation is close to the limits of the chosen CZM to simulate the present experiment.

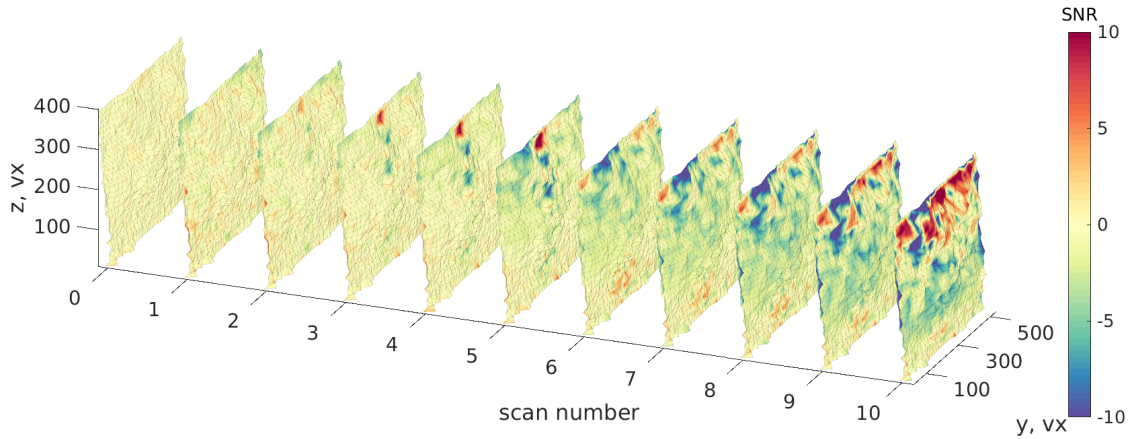


Figure 12: Displacement jump residual, in the x -direction, using the parameters after FEMU-F convergence. Positive residuals indicate that the opening measured via DVC was higher than that predicted by FE simulation

The analysis of the kinematic residuals underlines the benefit of using full-field 3D data. If only the loading curve shown in Figure 2(b) were to be simulated, the case with a straight crack path could be used. However, the calibrated parameters when the real crack path geometry was assessed gives insight into how much they may change under different hypotheses, let alone their variation between samples that was not discussed herein. Therefore, special care

Calibration of cohesive parameters for a refractory using 4D data and realistic crack path from in-situ WST should be taken for using such parameters for design purposes.

4.3. Dissipated energy

COD fields obtained from the FE simulation using the calibrated parameters are shown in Figure 13 for both crack paths. Since the prescribed boundary conditions were the same, these openings were expected to be very close. However, when the mesh was adapted to the actual crack path, the area with cohesive elements increased by about 12%. Conversely, the calibrated fracture energy J_c was 10% higher for the straight crack path (Table 3). Once J_c was multiplied by the cracked area, the difference was only 1% between both meshes. Moreover, the different calibrated parameters changed very significantly the openings in the traction-separation law. For instance, the cohesive elements in the straight mesh started to damage with 3.1 μm opening and dissipated energy up to 626 μm , while for the adapted mesh these levels changed to 3.9 μm and 782 μm , respectively. It is worth noting that damage initiated at opening levels slightly lower than the uncertainty in the present DVC analysis (Table 1) but could be evaluated with the presented strategy. As a reference, the COD fields assessed via DVC are shown in the third row of Figure 13 with the same dynamic range. The overall trends and levels are consistent [Figure 13(b-c)]. Yet, there were higher fluctuations in the experimental fields. These fluctuations are not due measurement uncertainties (Table 1) but are believed to be caused by the heterogeneous microstructure of the studied castable at the scale of Figures 3(a,b).

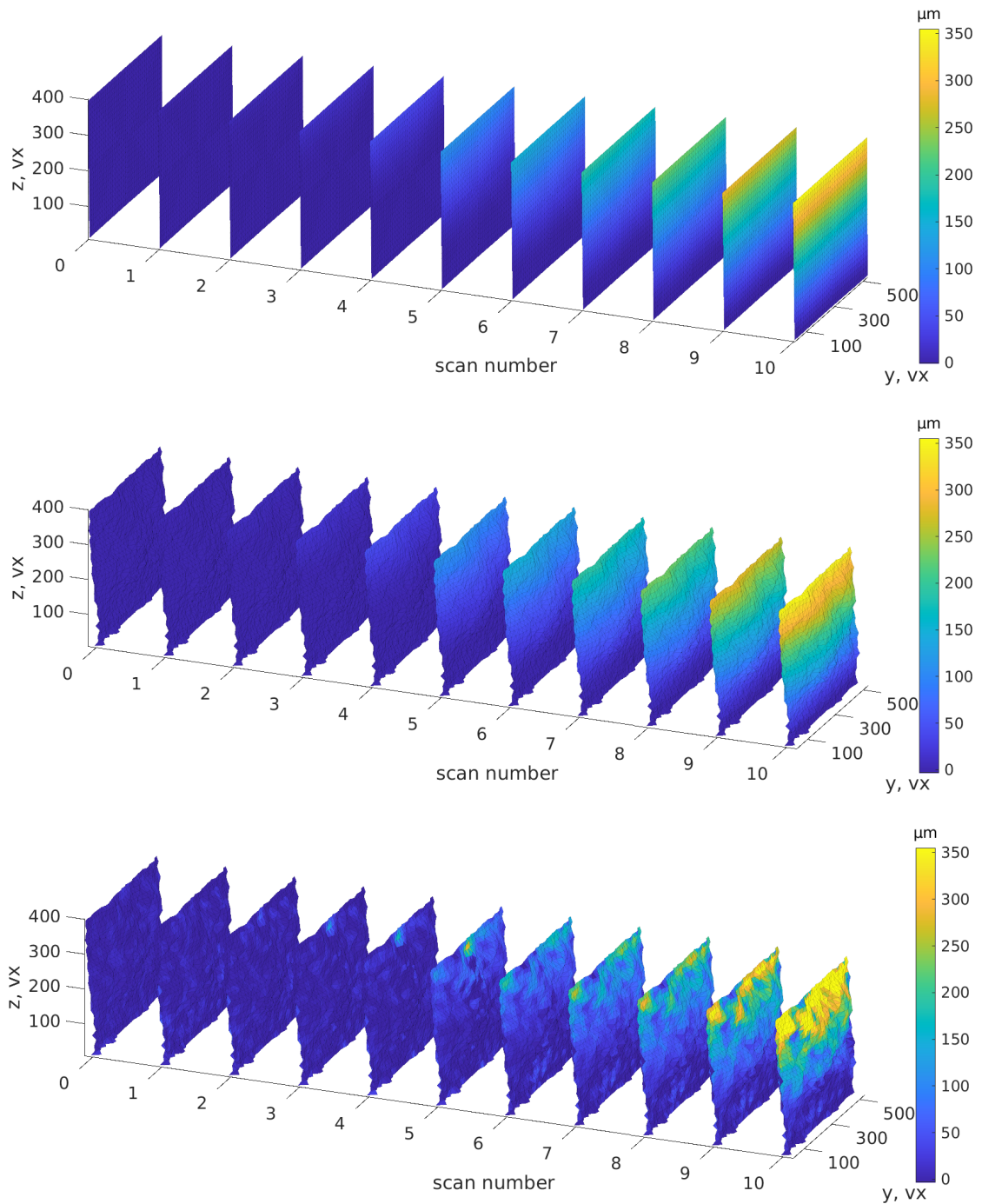


Figure 13: Crack Opening Displacement (COD) in the x -direction calculated for each cohesive element using the meshes with a straight (first row) or adapted (second row) crack path. The third row shows the measured COD fields via DVC using the adapted mesh.

When the normal tractions are investigated (Figure 14), their levels are very different. Their maximum amplitude

is about 40% higher as could be inferred from the calibrated cohesive strength σ_f (*i.e.*, 3.5 MPa for the straight crack path and 2.5 MPa for the adapted mesh)), although the fields are qualitatively very close in their temporal development. For scan #3, the row of cohesive elements closest to the pre-notch was already damaged. Right after the peak load (scan #5), cohesive elements below the mid-height of the sample were damaged and the initiation front started to be slowed down since it reached compressive zones at the very bottom of the sample.

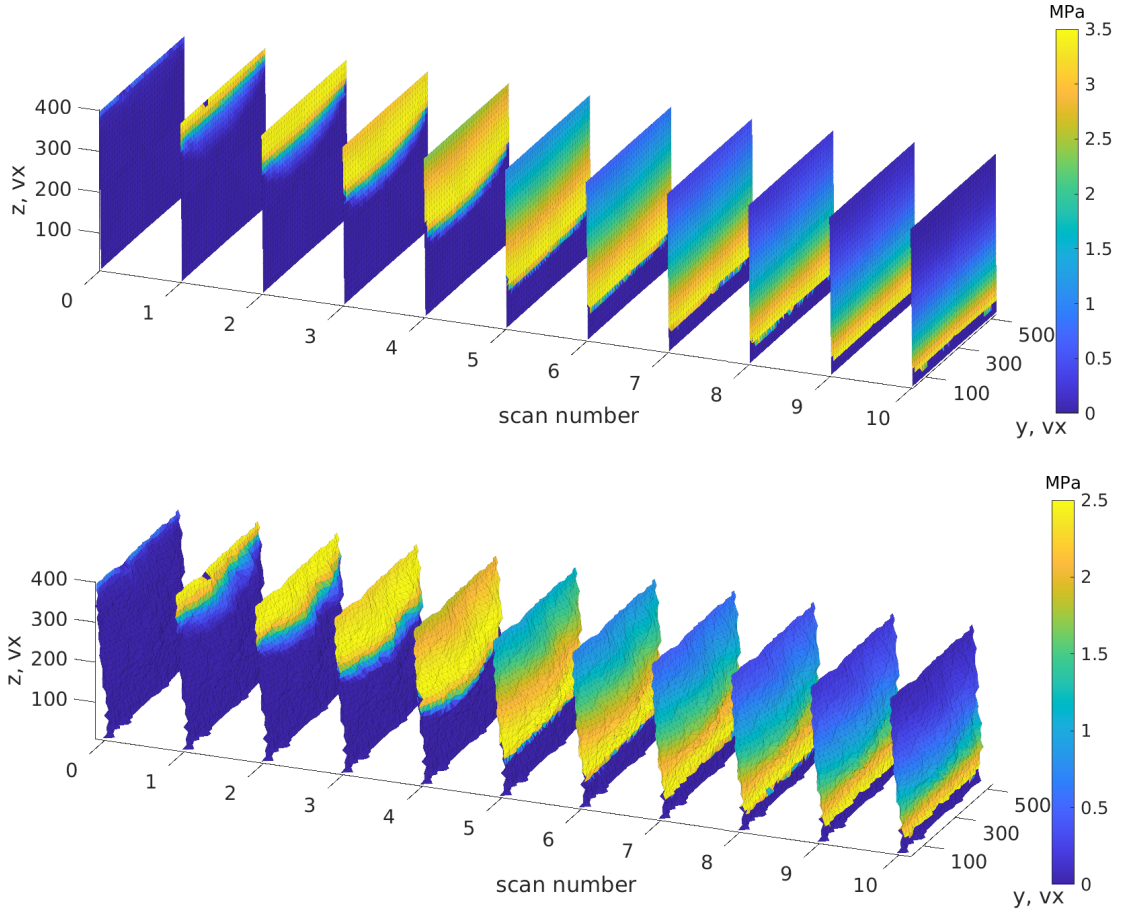


Figure 14: Tractions in the x-direction for each cohesive element using the mesh with straight (first row) or adapted (second row) crack path.

In the studied cases, the cumulated work was calculated and is reported in Figure 15. The work of fracture assessed by integrating the experimental actuator displacement vs. vertical forces gives an upper bound of the dissipated energy, since it considers the energy stored in the loading setup and other contributions such as friction. To consider only the work performed on the sample, the CMOD calculated via DVC was used together with the splitting force (*i.e.*, 5.715 times the vertical load). It is worth noting that both of these experimental works include the elastic energy stored in the sample, even if this energy should vanish as the crack propagates toward the end of the specimen.

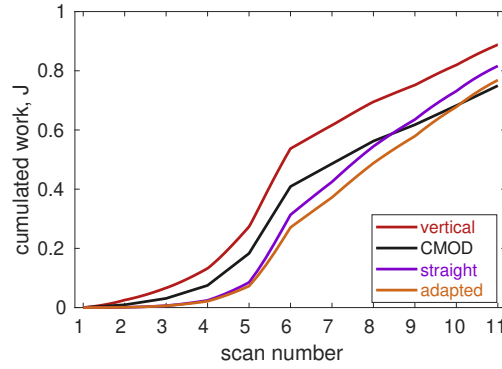


Figure 15: Cumulated work during the experiment assessed with four different approaches

For the cohesive elements, the overall work was calculated using the normal crack opening displacement and traction associated with the element area. The sum of all the elementary contributions in a given time step is reported in Figure 15 for both analyzed meshes. Up to scan #4, their contributions were very close, since the cohesive elements had little or no damage at all. Moreover, the work was lower than the experimental assessments since the necessary work to elastically load the remainder of the sample was not accounted for. In such case, they should converge to similar values at the end of the very experiment. Once damage has initiated, more energy was dissipated when the straight crack path was assumed. It also remains closer to the CMOD when the mesh adapted to the crack path is used.

From the cumulated work, the final elastic energy was removed to calculate the dissipated energy, which was then divided by the cracked area to evaluate the fracture energies reported in Table 4. Three different assumptions were considered for the cracked area. Method #1 (with $S_1 = 3550 \text{ mm}^2$) consists in the simplest choice of a full straight crack path along the full height. Conversely, $S_2 = 3280 \text{ mm}^2$ (*i.e.*, Method #2) and $S_3 = 3670 \text{ mm}^2$ (*i.e.*, Method #3) are the surface areas of the damaged cohesive elements for the straight and adapted meshes, respectively. All these values were less than the calibrated fracture energies J_c (Table 3) since there were many cohesive elements that were not fully damaged. The fracture energy in the case with a straight crack path is similar to that calculated using the applied force, which is an upper bound. The adapted mesh brings fracture energies closer to those computed from CMOD data, further validating the mesh adaption approach.

Table 4

Dissipated and fracture energies for three different methods of evaluation (see text)

	Dissipated energy, J	Method #1, J/mm ²	Method #2, J/mm ²	Method #3, J/mm ²
applied force	0.70	198	214	191
CMOD	0.60	169	183	163
straight	0.69	–	212	–
adapted	0.62	–	–	170

Even though cohesive elements are used to simulate quasi-brittle fracture in which toughening mechanisms take place, care should be taken since most of the fracture energies gathered in Table 4 overestimated that associated with the adapted mesh. If only the dissipated energy is sought, similar results were obtained by the simpler choice of using CMOD data with the assumption of a straight crack path.

5. Conclusion

The fracture of an alumina castable refractory with mullite-zirconia aggregates was investigated with an in-situ WST. Several tomographic scans were acquired during the experiment and the reconstructed 3D images were analyzed via FE-based DVC, which gave access to measurement uncertainties, to a Lagrangian and realistic crack path, and to proper boundary conditions for 4D (*i.e.*, 3D space and time) FE simulations of the whole sample. The experimental force was used in the cost function to be minimized after checking that the chosen parameters had low sensitivity with respect to kinematic measurements (*i.e.*, below their uncertainty levels). The measured full-field displacements and gray level residuals provided valuable information to check the trustworthiness of the simulations using cohesive elements and the hypothesis of straight or adapted crack paths, using the same meshes for DVC measurements and FE simulations.

Both geometrical hypotheses provided very good and indistinguishable descriptions of the experimental forces with errors of only about seven times the load cell uncertainty even though very different cohesive parameters were calibrated. Although the Young's modulus and the correction for the boundary conditions were similar whether a straight or a realistic crack path was employed, the cohesive strength was 35% higher and the fracture energy 10% higher for the former case. Conversely, they could be distinguished by the kinematic residuals. Using the experimental crack path revealed by the DVC residuals, the overall displacement residual was of the order of seven times and the COD around five times the corresponding uncertainties. For the straight crack path, three units higher were observed for both quantities, which are significant. Smaller DVC residuals were found when the mesh was adapted to describe the cracked surface, further proving the validity of the FE simulation.

A general FEMU approach was followed in a way that it could be applied to very different cases by changing the material, geometry, constitutive law or even the quantities in the minimized cost-function for parameter calibration. The variation of the calibrated parameters for different samples also remains to be checked. Such framework using in-situ WSTs and DVC may also be used for comparing the resultant crack paths in the bulk of materials with different compositions, which is specially useful for investigating toughening mechanisms such as crack deflection or branching.

Acknowledgments

This study was supported in part by #2018/23081-0, #2020/08077-6, and #2021/09238-6 projects from São Paulo Research Foundation (FAPESP), by the French “Agence Nationale de la Recherche” through the “Investissements d’avenir” program (ANR-10-EQPX-37 MATMECA Grant), and by the Coordenação de Aperfeiçoamento de Pessoal de Nível Superior - Brasil (CAPES) - Finance Code 001 CAPES (Brazil). The authors would like to thank IBAR (Indústrias Brasileiras de Artigos Refratários, Poá, Brazil) for kindly providing the materials, and Prof. J.A. Rodrigues for stimulating discussions about various aspects of WSTs.

Credit authorship statement

R. Vargas: Conceptualization, Methodology, Investigation, Software, Original draft preparation, Writing - Review & Editing

R.B. Canto: Supervision, Conceptualization, Writing - Review & Editing, Resources, Funding acquisition, Project administration

B. Smaniotto: Methodology, Investigation, Data Curation, Visualization

F. Hild: Supervision, Conceptualization, Methodology, Software, Formal analysis, Writing - Review & Editing, Resources, Funding acquisition, Project administration

Declaration of Competing Interest

The authors declare that they have no known competing financial interests or personal relationships that could have appeared to influence the work reported in this paper.

References

- [1] J. Wachtman, Materials and Equipment - Whitewares - Refractory Ceramics - Basic Science: Ceramic Engineering and Science Proceedings, Volume 16, no. 1 in Ceramic Engineering and Science Proceedings, Wiley, 2009.
- [2] W. E. Lee, W. Vieira, S. Zhang, K. Ghanbari Ahari, H. Sarpoolaky, C. Parr, Castable refractory concretes, International Materials Reviews 46 (3) (2001) 145–167.
- [3] A. P. Luz, M. A. L. Braulio, V. C. Pandolfelli, Refractory Castable Engineering, 1st Edition, Vol. 1, Göller Verlag, São Carlos, SP, 2015.
- [4] W. E. Lee, R. E. Moore, Evolution of in situ refractories in the 20th century, Journal of the American Ceramic Society 81 (6) (1998) 1385–1410.
- [5] A. Hillerborg, M. Modéer, P. E. Petersson, Analysis of crack formation and crack growth in concrete by means of fracture mechanics and finite elements, Cement and Concrete Research 6 (6) (1976) 773–782.
- [6] A. Hillerborg, Analysis of one single crack, in: Fracture Mechanics of Concrete (Developments in civil engineering), Elsevier, 1983, pp. 223–249.
- [7] B. Cotterell, S. W. Ong, C. Qin, Thermal shock and size effects in castable refractories, Journal of the American Ceramic Society 78 (8) (1995) 2056–2064.
- [8] K. Andreev, H. Harmuth, FEM simulation of the thermo-mechanical behaviour and failure of refractories—a case study, Journal of Materials Processing Technology 143 (2003) 72–77.
- [9] S. Jin, D. Gruber, H. Harmuth, R. Rössler, Thermomechanical failure modeling and investigation into lining optimization for a Ruhrstahl Heraeus snorkel, Engineering Failure Analysis 62 (2016) 254–262.
- [10] D. Gruber, H. Harmuth, A laser irradiation disc test for fracture testing of refractory fine ceramics, Journal of the European Ceramic Society 34 (15) (2014) 4021–4029.
- [11] S. Samadi, S. Jin, D. Gruber, H. Harmuth, A comparison of two damage models for inverse identification of mode I fracture parameters: Case study of a refractory ceramic, International Journal of Mechanical Sciences 197 (2021) 106345.
- [12] J.-D. Mathias, N. Tessier-Doyen, Homogenization of glass/alumina two-phase materials using a cohesive zone model, Computational materials science 43 (4) (2008) 1081–1085.
- [13] X.-P. Xu, A. Needleman, Numerical simulations of fast crack growth in brittle solids, J. Mech. Phys. Solids 42 (1994) 1397–1434.
- [14] I. Özdemir, W. A. M. Brekelmans, M. G. D. Geers, Modeling thermal shock damage in refractory materials via direct numerical simulation (DNS), Journal of the European Ceramic Society 30 (7) (2010) 1585–1597.
- [15] M. van den Bosch, P. Schreurs, M. Geers, An improved description of the exponential xu and needleman cohesive zone law for mixed-mode decohesion, Eng. Fract. Mech. 73 (2006) 1220–1234.
- [16] M. A. J. Van Gils, L. J. M. G. Dortmans, G. De With, W. A. M. Brekelmans, J. H. P. De Vree, Size effect predictions by fracture models for a refractory ceramic, International journal of fracture 75 (3) (1996) 273–283.
- [17] S. Heinz, J. Tu, M. Jackson, J. Wiggins, Digital image correlation analysis of strain recovery in glassy polymer network isomers, Polymer 82 (2016) 87–92.
- [18] L. Pan, Z. He, Y. Li, B. Li, S. Jin, Inverse simulation of fracture parameters for cement-bonded corundum refractories, JOM 71 (11) (2019) 3996–4004.
- [19] G. Alfano, M. A. Crisfield, Finite element interface models for the delamination analysis of laminated composites: mechanical and computational issues, International journal for numerical methods in engineering 50 (7) (2001) 1701–1736.
- [20] A. Doitrand, R. Estevez, M. Thibault, P. Leplay, Fracture and cohesive parameter identification of refractories by Digital Image Correlation up to 1200 °C, Experimental Mechanics 60 (5) (2020) 577–590.

- [21] R. Vargas, J. Neggers, R. B. Canto, J. A. Rodrigues, F. Hild, Analysis of a castable refractory using the wedge splitting test and cohesive zone model, *Journal of the European Ceramic Society* 39 (13) (2019) 3903–3914.
- [22] R. Vargas, R. B. Canto, F. Hild, Fracture energy evaluation of refractories in wedge splitting tests from notch opening displacements, *Journal of the European Ceramic Society* 41 (10) (2021) 5367–5379.
- [23] R. Vargas, R. Canto, F. Hild, On the calibration of cohesive parameters for refractories from notch opening displacements in wedge splitting tests, *Journal of the European Ceramic Society* 41 (14) (2021) 7348–7361.
- [24] M. Mostafavi, S. A. McDonald, P. M. Mummery, T. J. Marrow, Observation and quantification of three-dimensional crack propagation in poly-granular graphite, *Engineering Fracture Mechanics* 110 (2013) 410–420.
- [25] M. Mostafavi, N. Baimpas, E. Tarleton, R. C. Atwood, S. A. McDonald, A. M. Korsunsky, T. J. Marrow, Three-dimensional crack observation, quantification and simulation in a quasi-brittle material, *Acta Materialia* 61 (16) (2013) 6276–6289.
- [26] D. Gonzalez, A. King, M. Mostafavi, P. Reischig, S. Rolland du Roscoat, W. Ludwig, J. Quinta da Fonseca, P. J. Withers, T. J. Marrow, Three-dimensional observation and image-based modelling of thermal strains in polycrystalline alumina, *Acta materialia* 61 (20) (2013) 7521–7533.
- [27] E. Ferrié, J. Buffière, W. Ludwig, A. Gravouil, L. Edwards, Fatigue crack propagation: In situ visualization using x-ray microtomography and 3d simulation using the extended finite element method, *Acta Mat.* 54 (4) (2006) 1111–1122.
- [28] J. Rannou, N. Limodin, J. Réthoré, A. Gravouil, W. Ludwig, M. Baïetto, J. Buffière, A. Combescure, F. Hild, S. Roux, Three dimensional experimental and numerical multiscale analysis of a fatigue crack, *Comp. Meth. Appl. Mech. Eng.* 199 (2010) 1307–1325.
- [29] J. Réthoré, N. Limodin, J. Buffière, F. Hild, W. Ludwig, S. Roux, Digital volume correlation analyses of synchrotron tomographic images, *J. Strain Analysis* 46 (2011) 683–695.
- [30] V. Maurel, V. Chiaruttini, M. Abecassis, A. Koster, S. Dezecot, Influence of a 3D realistic crack path in the driving forces for fatigue crack growth under mode I + II loading, *Theoretical and Applied Fracture Mechanics* 108 (2020) 102570.
- [31] R. Vargas, R. B. Canto, F. Hild, Cohesive properties of refractory castable at 600°C: Effect of sintering and testing temperature, *Journal of the European Ceramic Society* (Published Online) (2022).
- [32] C. Jailin, A. Bouterf, R. Vargas, F. Hild, S. Roux, Sub-minute In Situ Fracture Test in a Laboratory CT Scanner, *Integrating Materials and Manufacturing Innovation* 8 (3) (2019) 413–422.
- [33] R. Vargas, X. Pinelli, B. Smaniotto, F. Hild, R. B. Canto, On the effect of sintering temperature on fracture energy of Alumina-Mullite-Zirconia castable at 600°C, *Journal of the European Ceramics Society* 41 (7) (2021) 4406–4418.
- [34] E. Tschegg, Prüfeinrichtung zur Ermittlung von bruchmechanischen Kennwerten sowie hierfür geeignete, Prüfkörper, *Austrian Pat. AT 390328B*, registered (1986).
- [35] A. Buljac, T. Taillandier-Thomas, L. Helfen, T. Morgeneyer, F. Hild, Evaluation of measurement uncertainties of digital volume correlation applied to laminography data, *Journal of Strain Analysis for Engineering Design* 53 (2018) 49–65.
- [36] F. Hild, A. Bouterf, L. Chamoin, F. Mathieu, J. Neggers, F. Pled, Z. Tomičević, S. Roux, Toward 4d mechanical correlation, *Adv. Mech. Simul. Eng. Sci.* 3 (1) (2016) 1–26.
- [37] H. Leclerc, J. Neggers, F. Mathieu, S. Roux, F. Hild, Correli 3.0, IDDN.FR.001.520008.000.S.P.2015.000.31500 (2015).
- [38] P. Auger, T. Lavigne, B. Smaniotto, M. Spagnuolo, F. Dell’Isola, F. Hild, Poynting Effects in Pantographic Metamaterial Captured via Multi-scale DVC, *Journal of Strain Analysis for Engineering Design* 56 (7) (2021) 462–477.
- [39] C. Geuzaine, J.-F. Remacle, Gmsh: A 3D finite element mesh generator with built-in pre-and post-processing facilities, *International Journal for Numerical Methods in Engineering* 79 (11) (2009) 1309–1331.
- [40] A. Mendoza, J. Neggers, F. Hild, S. Roux, Complete mechanical regularization applied to digital image and volume correlation, *Computer*

Methods in Applied Mechanics and Engineering 355 (2019) 27–43.

- [41] K. Park, G. H. Paulino, J. R. Roesler, A unified potential-based cohesive model of mixed-mode fracture, *Journal of the Mechanics and Physics of Solids* 57 (6) (2009) 891–908.
- [42] D. W. Spring, G. H. Paulino, A growing library of three-dimensional cohesive elements for use in abaqus, *Engineering Fracture Mechanics* 126 (2014) 190–216.
- [43] K. Kavanagh, R. Clough, Finite element applications in the characterization of elastic solids, *Int. J. Solids Struct.* 7 (1971) 11–23.
- [44] F. Hermez, C. Farhat, Updating finite element dynamic models using element-by-element sensitivity methodology, *AIAA Journal* 31 (9) (1993) 1702–1711.
- [45] E. Pagnacco, A. Caro-Bretelle, P. Jenny, *Parameter Identification from Mechanical Field Measurements using Finite Element Model Updating Strategies*, ISTE / Wiley, London (UK), 2012, pp. 247–274.
- [46] F. Mathieu, H. Leclerc, F. Hild, S. Roux, Estimation of elastoplastic parameters via weighted FEMU and integrated-DIC, *Exp. Mech.* 55 (1) (2015) 105–119.
- [47] A. Tikhonov, V. Arsenin, *Solutions of ill-posed problems*, J. Wiley, New York (USA), 1977.
- [48] H. Leclerc, J. Neggers, F. Mathieu, F. Hild, S. Roux, *Correli 3.0*, IDD.N.FR.001.520008.000.S.P.2015.000.31500, Agence pour la Protection des Programmes, Paris (France) (2015).

Appendix A: DVC hardware and analysis parameters

All the hardware parameters for the tomograph and the testing machine in which the experiments were performed are reported in Table 5.

Table 5

DVC hardware parameters

Tomograph	North Star Imaging X50+
X-ray source	XRyWorX XWT-240-CT
Target / Anode	Tungsten (reflection mode)
Filter	none
Voltage	200 kV
Current	400 μ A
Focal spot size	5 μ m
Tube to detector	505 mm
Tube to object	226 mm
Detector	Dexela 2923
Definition	1536 \times 1944 pixels (2 \times 2 binning)
Number of projections	1000
Angular amplitude	360°
Frame average	10 per projection
Frame rate	10 fps
Acquisition duration	about 17 min (continuous rotation mode)
Reconstruction algorithm	filtered back-projection
Gray Level amplitude	8 bits
Volume size	554 \times 568 \times 677 voxels (after 2 \times 2 \times 2 binning and crop)
Field of view	74.6 \times 76.5 \times 91.1 mm ³ (after 2 \times 2 \times 2 binning and crop)
Image scale	135 μ m/voxel
Testing machine	Deben TTC
Load cell capacity	\pm 20 kN
Actuator velocity	1 μ m/s
Force uncertainty	1.4 N (standard deviation of acquisition on unloaded frame)

The software parameters for the DVC analyzes are gathered in Table 6.

Table 6

DVC analysis parameters

DVC software	Correli 3.0 [48]
Image filtering	none
Element length (mean)	27 and 18 vx
Shape functions	linear (T4 elements) [36]
Meshes	see Figures 3 and 4
Matching criterion	penalized sum of squared differences
Convergence criterion	RMS of nodal displacement correction $\leq 10^{-4}$ vx
Regularization length	$\ell_{reg} = 10$ vx
Interpolant	cubic
Displacement noise floor	1 and 3 cvx

Appendix B: Displacement sensitivities

The sensitivities of the opening (*i.e.*, in the x -direction) displacements can also be calculated as

$$\left[\hat{\mathbf{S}}_{u_x} \right] = \frac{1}{\gamma_u} \left[\delta u_{x\text{FE}}(t, \{\mathbf{p}_0\}) \right] \quad (13)$$

and is shown for the studied parameters in Figure 16. The sensitivities for the other two directions were at least five times smaller and thus are not shown. Qualitatively, the trends are very similar to those of COD sensitivities (Section 3.3.5). Globally, the displacement sensitivities remained very low, namely, of the order of one hundredth of the uncertainty levels (for a 1% variation of the parameters), but their qualitative trends help understand their influence on the simulated kinematics. When the Young's modulus was increased (first row of Figure 16), the opening was increased first at the pre-notch and went down the sample for the latter scans since higher rigidity promotes earlier development of damage. The BCc parameter (second row in Figure 16) was the most sensitive parameter, as expected, especially in the top regions where the boundary conditions were applied. The increase of the cohesive strength (third row of Figure 16) induced crack closure up to scan #5 (*i.e.*, positive sensitivity on the left part of the sample) and then more opening at the end. This effect is due to the fact that an increased cohesive strength σ_f , *ceteris paribus*, delayed the initiation of damage but once it started, energy dissipation was possible for smaller openings. Last, increasing the fracture energy (see last row in Figure 16) tended to hinder crack opening.

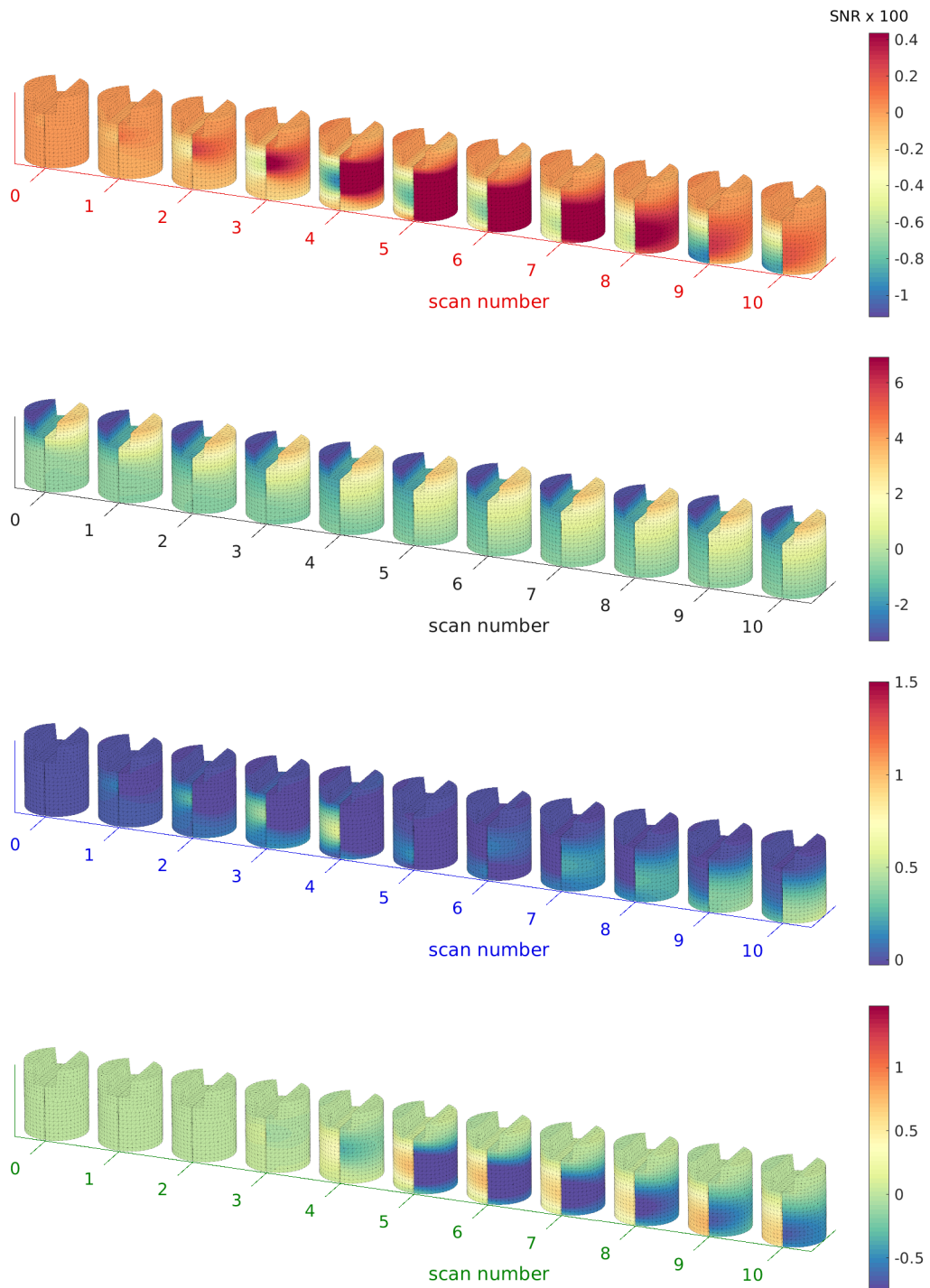


Figure 16: Sensitivity fields for the displacements in the x -direction (\hat{S}_{u_x}) for a 1% variation of the parameters E (top row), BCc (second row), σ_f (third row), and J_c (bottom row)

The associated normalized Hessian matrix reads

$$[\hat{\mathbf{H}}_{\mathbf{u}_x}] = \frac{1}{N_{t_u} N_n} [\hat{\mathbf{S}}_{u_x}]^\top [\hat{\mathbf{S}}_{u_x}] \quad (14)$$

and is presented in Figure 17 along its eigen decomposition. The biggest difference from COD sensitivities was on the BCc parameter that is dominating the first eigen parameter. Yet, the overall sensitivities remained very low.

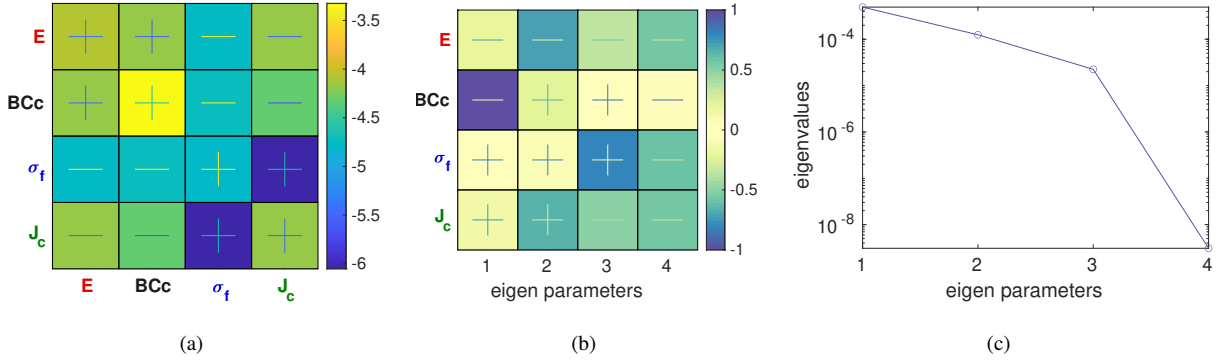


Figure 17: Normalized Hessians for the x -displacement in decimal logarithm (a) together with their eigen decomposition. The eigen parameters are shown in sub-figure (b) and the corresponding eigenvalues in (c).